JACS
JOURNAL OF THE AMERICAN CHEMICAL SOCIETY

Article

pubs.acs.org/JACS

$Au_{24}(SAdm)_{16}$ Nanomolecules: X-ray Crystal Structure, Theoretical Analysis, Adaptability of Adamantane Ligands to Form $Au_{23}(SAdm)_{16}$ and $Au_{25}(SAdm)_{16}$, and Its Relation to $Au_{25}(SR)_{18}$

David Crasto,[†] Giovanni Barcaro,[‡] Mauro Stener,[§] Luca Sementa,[‡] Alessandro Fortunelli,*[,‡] and Amala Dass*[,†]

[†]Department of Chemistry and Biochemistry, University of Mississippi, Oxford, Mississippi 38677, United States
[‡]CNR-ICCOM & IPCF, Consiglio Nazionale delle Ricerche, Pisa I-56124, Italy
[§]Dipartimento di Scienze Chimiche e Farmaceutiche, Università di Trieste, Trieste I-34127, Italy

Supporting Information

ABSTRACT: Here we present the crystal structure, experimental and theoretical characterization of a $Au_{24}(SAdm)_{16}$ nanomolecule. The composition was verified by X-ray crystallography and mass spectrometry, and its optical and electronic properties were investigated via experiments and first-principles calculations. Most importantly, the focus of this work is to demonstrate how the use of bulky thiolate ligands, such as adamantanethiol, versus the commonly studied phenylethanethiolate ligands leads to a great structural flexibility, where the metal core changes its shape from five-fold to crystalline-like motifs and can adapt to the formation of $Au_{24\pm1}(SAdm)_{16}$, namely, $Au_{23}(SAdm)_{16}$, $Au_{24}(SAdm)_{16}$, and $Au_{25}(SAdm)_{16}$. The basis for the construction of a thermodynamic phase diagram of Au nanomolecules in terms of ligands and solvent features is also outlined.

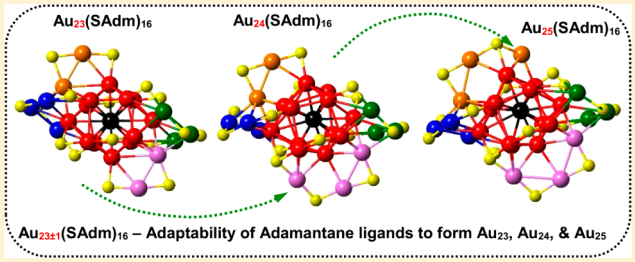

INTRODUCTION

Gold nanomolecules, also called nanocrystal gold molecules,[1] or monolayer-protected cluster molecules,[2] are chemical entities in the 1−3 nm size range with chemical formula $Au_x(SR)_y$, for which a fixed number of gold atoms, x, are stabilized by a given number of sulfur ligands, y.[1,3−5] This was first confirmed by the crystal structure report on $Au_{102}(p\text{-MBA})_{44}$,[6] followed by the crystal structure characterization of $Au_{25}(SR)_{18}$.[7] Nanomolecules protected by aliphatic thiols of the form $C_nH_{2n+1}SH$, or phenylethanethiol,[8] include $Au_{25}(SR)_{18}$, $Au_{38}(SR)_{24}$, $Au_{67}(SR)_{35}$, and $Au_{144}(SR)_{60}$,[9−11] followed by plasmonic Faradaurate-329, -500, and -940, with compositions of $Au_{329}(SR)_{84}$, $Au_{\sim500\pm10}(SR)_{\sim120\pm3}$, and $Au_{\sim940\pm20}(SR)_{\sim160\pm4}$.[12−14] The optical properties of these systems range from molecule-like features with distinct electronic transitions to surface plasmon resonances, where collective oscillations of conduction electrons are observed.

We showed that using an aromatic ligand, HS−C_6H_4−R (R = H) to prepare nanomolecules resulted in a new 36-atom core,[15] not the well-known 38-atom core.[9,16] By varying the R group, others have confirmed the 36-atom core and reported that the $Au_{36}(SC_6H_4\text{-}tBu)_{24}$ has a fcc-like core,[17] unlike the bi-icosahedral $Au_{38}(SR)_{24}$ structure. Using bulky ligands such as cyclohexanethiol (HSCy) and adamantanethiol (HSAdm), Tracy's group[18] reported the preparation of $Au_{30}(SAdm)_{18}$, $Au_{39}(SAdm)_{23}$, $Au_{65}(SCy)_{30}$ and $Au_{67}(SCy)_{30}$. Tsukuda's group reported the synthesis of $Au_{42}(SEind)_{12}$, where SEind is a bulky arene thiol.[19] Building on these early reports, crystal structure and synthesis of some of the bulky ligated systems were reported recently.[20−22] The atomic structure of $Au_{23}(SCy)_{16}$ was reported to contain a Au_{13} cuboctahedral core capped by two atoms to form a bipyramidal Au_{15} kernel, protected by two trimeric $-Au_3(SR)_4-$ motifs and two monomeric $-Au(SR)_2-$ motifs and four bridging SR ligands.[20] The crystal structure of $Au_{30}S(StBu)_{18}$ was shown to contain a Au_{20} bi-cuboctahedral core capped by two atoms to form a Au_{22} core, protected by two monomeric, two trimeric and six bridging SR ligands.[21] The crystal structure reports show that bulky ligands not only change the composition, but also the atomic structure. The 25-atom nanomolecules possess an icosahedral core, whereas the 23- and 30-atom nanomolecules are based on cuboctahedral cores. However, there is a lack in our understanding of the reasons for the change in atomic structure, and especially in the interplay of energetic and kinetic factors.

Here, we report (a) the crystal structure and theoretical analysis of a novel $Au_{24}(SAdm)_{16}$ compound; (b) a computational study of the energetics of icosahedral $Au_{25}(SR)_{18}$ versus cuboctahedral $Au_x(SR)_{16}$ (x = 23, 24, 25) systems; and (c) the greater flexibility in local composition and geometry associated with bulky ligated systems. This means that, while the composition of $Au_{25}(SR)_{18}$ is robust and fixed, the composition

Received: July 29, 2014
Published: October 13, 2014

   dx.doi.org/10.1021/ja507738e | J. Am. Chem. Soc. 2014, 136, 14933−14940

of bulky ligated system are flexible, $Au_{24\pm1}(SR)_{16}$ is possible, to form $Au_{23}(SAdm)_{16}$, $Au_{24}(SAdm)_{16}$ and $Au_{25}(SAdm)_{16}$, as proven by mass spectrometry and DFT calculations. Finally, (d) we propose a thermodynamic analysis of Au nanomolecules as a function of coating species and environmental variables aimed at eventually drawing a phase diagram that can help orient the synthesis of such compounds.

EXPERIMENTAL SECTION

Synthesis. Synthesis involved three steps. First, a crude product containing polydisperse 1-adamantanethiolate protected Au clusters was prepared in a modification of a reported process.[23] Second, solvent fractionation was used to isolate pure monodisperse nanomolecules.[24] Finally, Au_{24} nanomolecule crystals were obtained by crystallization from vapor−vapor diffusion from an ethanol-toluene solvent system.

In step 1, 20 mL of THF containing 100 mg $HAuCl_4{\cdot}3H_2O$ is initially combined with 98.8 mg (0.588 mmol) of 1-adamantanethiol for a 1:3 mole ratio. No TOABr, or any other additives were introduced into the reaction flask. After stirring at 450 rpm for 15 min, 110 mg of $NaBH_4$ (dissolved in 5 mL of cold, distilled H_2O) was then added instantaneously, turning the light-yellow mixture to the characteristic black color observed in nanoparticle crude mixtures. The reaction mixture is then continued stirring for an additional 1 h, after which the product was collected and rotary-evaporated to dryness in order to remove the THF solvent. After using sequential rounds of MeOH cleansing and centrifugation, the nanoparticles were purified of any excess thiol present from the reaction.

In step 2, ∼40 mg of crude product after cleaning/drying is added to 15−20 mL of acetone. The 20 mL screw-cap vial is then centrifuged, which separated into a distinct soluble layer, and insoluble precipitate. The soluble layer is transferred to a separate vial and subject to rotary evaporation to remove the acetone solvent. This process is repeated a total of three times in order to obtain purely acetone-soluble material without any insoluble material left over.

In step 3, to further purify the material, vapor diffusion of an insoluble ethanol portion into a soluble portion of the nanoparticles in toluene is conducted for crystallizing the material. After 5−7 days, brown plate-like crystals were observed at the bottom of the soluble portion.

Mass Spectrometry and Optical Spectroscopy. ESI-MS was measured using Waters Synapt HDMS instrument. The crystalline material was harvested from the mother liquor and, after first being washed with MeOH, is dissolved in 90:10 v/v toluene:EtOH. Data collection was also performed with MeOH as the solvent additive in toluene (90:10 again), in order to reproduce the m/z 3701 peak representative of the 2+ of $Au_{24}(SAdm)_{16}$.

X-ray Crystallography. Crystalline material of $Au_{24}(SAdm)_{16}$ was obtained as follows: ∼1.0 mg of acetone-soluble product was dissolved in toluene in a 4 mL vial. In a separate 20 mL vial, an insoluble ethanol bath then encompasses the 4 mL vial placed carefully in the middle. After screwing the cap to the 20 mL vial tightly, the crystallization apparatus is then allowed to sit out of direct light in a cabinet undisturbed for 5−7 days, after which brown plate-like crystalline material was observed. These were then transferred from the vial onto a microscope slide in order to immerse in oil. The crystals were viewed under a polarizing microscope and selected from the oil under ambient conditions and attached to the tip of a MiTeGen MicroMount. The crystal was mounted in a stream of cold nitrogen and centered in the X-ray beam by using a video camera. Data collection and crystal analysis were performed on a Bruker APEX II diffractometer with Mo Kα (λ = 0.71073 Å) radiation. Using Olex2,[25] the structure was solved with the XT structure solution program and refined with the XL refinement package using Least Squares minimization.

Crystal Data. For $C_{160}H_{240}Au_{24}S_{16}$ (MW = 7403.66): triclinic, space group $P\bar{1}$ (No. 2), a = 16.362(3) Å, b = 19.900(3) Å; c = 32.189(5) Å, α = 89.736(9)°, β = 77.790(8)°, γ = 80.239(9)°, V = 10090(3) Å^3, Z = 2, μ(Mo Kα) = 17.571 mm^{-1}; D_{calc} =2.437 mg/mm^3, F(000) = 6704; T = 100 K; 90 503 reflections measured ($1.3 \leq 2\theta \leq 45.98$), 27 803 unique ($R_{int}$ = 0.0549) reflections. Data/restraints/parameters = 27 803/4080/1001. Goodness-of-fit on F^2 = 1.047. The final R_1 was 0.0519 ($I > 2\sigma(I)$), and wR_2 was 0.1797 (all data). −2.55 < Δp < 1.79 e/Å^3. CCDC number 996445.

Computational Method. DFT local relaxations were carried out using the Quantum Espresso (QE) Plane Wave Self Consistent Field (PWscf) code[26] employing a basis set of plane waves, ultrasoft pseudopotentials[27] and the Perdew−Burke−Ernzerhof (PBE) exchange-correlation (xc) functional.[28] Values of 20 and 200 Ry were chosen as the energy cutoff for the selection of the plane waves for the description of the wave function and the electronic density, respectively. The first Brillouin zone was k-sampled at the gamma point only by employing a Gaussian broadening of the one-particle levels of about 0.03 eV. All the calculations were performed spin-polarized by using a simple cubic unit cell with size 50 au (1 au = 0.52918 Å).

Ab initio molecular dynamics (MD) was performed using the CP2K code,[29] whose DFT algorithms are based on a hybrid Gaussian/Plane-Wave (GPW) scheme.[30] The PBE xc-functional was employed as in the local minimizations. We chose pseudopotentials derived by Goedecker, Teter, and Hutter (GTH) to describe the core electrons of all atoms[31] and DZVP basis sets[32] to represent the DFT Kohn−Sham orbitals. The cutoff for the auxiliary plane wave representation of the density was 300 Ry. Each dynamics was followed for 5−10 ps with a time step of 1.0 fs during which the temperature is controlled by Nosé−Hoover chain thermostats.[33]

The optical spectrum was simulated by performing time-dependent DFT (TD-DFT) calculations with the Amsterdam density-functional (ADF) code.[34,35] The TD-DFT equations were solved within the Casida approach.[36] The basis set consisted of Slater Type Orbitals (STO) of triple-zeta plus two polarization functions for Au, C, and S atoms, while for H a double-zeta plus polarization set was employed. LB94 exchange-correlation potential[37] was used, due to its correct asymptotic behavior.

The following protocol was used for predicting the structure of $Au_{24}(SAdm)_{16}$. Local minimizations were first conducted on a complete atomistic model of $Au_{24}(SAdm)_{16}$. Starting from the experimentally determined X-ray crystal structure geometry, we performed a structural optimization of the entire structure and then a short run of ab initio MD to check that the derived model represented a local minimum. The atomic positions in the thus-obtained structure do not present significant changes with respect to those determined experiementally. Analogously, a starting structural model of $Au_{23}(SCy)_{16}$ was derived from ref 20 and subjected to a similar protocol, first using cyclohexanethiol ligands and then replacing these with adamantanethiols, while a similar procedure generated the geometry of $Au_{25}(SCH_2CH_2Ph)_{18}$ from which replacement of ethyphenyl residues with adamantyls and cyclohexyls produced the corresponding $Au_{25}(SR)_{18}$ compounds. As no crystallographic information was available for $Au_{25}(SR)_{16}$ nanomolecules, starting structural models of $Au_{25}(SAdm)_{16}$ and $Au_{25}(SCy)_{16}$ were obtained by adding a Au atom to $Au_{24}(SAdm)_{16}$ and $Au_{24}(SCy)_{16}$, respectively, and subjecting the resulting geometrical structure to the relaxation protocol described above. Geometries of $Au_{24\pm1}(SR)_{16}$ and $Au_{25}(SR)_{18}$ clusters were also derived with R = methyl. The atomic coordinates of Au, S, and C atoms were taken from the corresponding $Au_{24\pm1}(SR)_{16}$ and $Au_{25}(SR)_{18}$ relaxed geometries (with R = cyclohexyl, adamantyl, or ethyphenyl), adding hydrogen atoms as appropriate, and optimizing first their positions, and then the entire cluster geometry. It should be noted that in the following electronic energies—together with solvation energies, see below—are used to determine thermodynamic stability, neglecting rotovibrational enthalpic and entropic contributions.

In the Supporting Information, solvation energies of small charged species (such as Au^+ and Br^-) are calculated using a polarizable continuum model (PCM) approach with parameters appropriate for methanol as the solvent. The PCM model is the one implemented in the Gaussian09 code.[38] The corresponding electronic structures were calculated using a DFT/PBE approach with LANL2DZ effective core potentials and double-ζ polarized basis sets.[39] Solvation energies were neglected in the case of neutral species. Solvation energies of charged

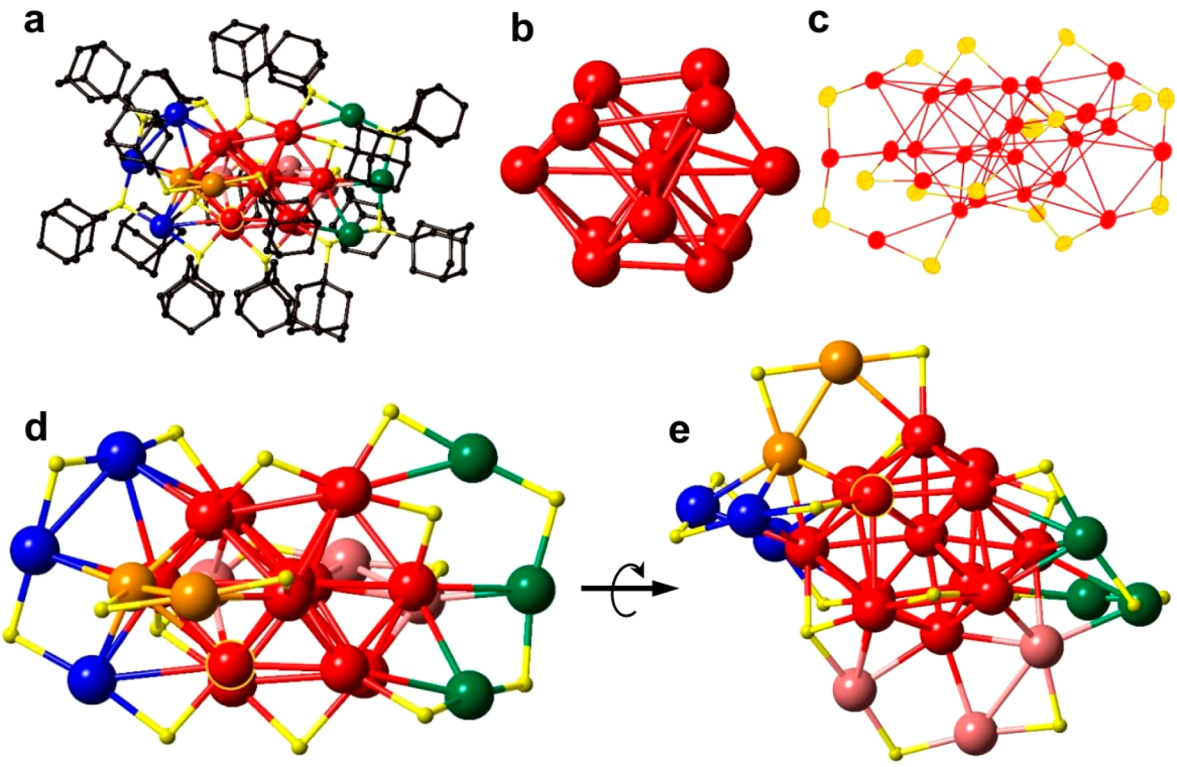

Figure 1. X-ray crystal structures of $Au_{24}(SAdm)_{16}$. (a) Total structure, with hydrogen atoms omitted for clarity. (b) Au_{13} cuboctohedral core. (c) $Au_{24}S_{16}$ structure displayed as thermal ellipsoids showing the quality of anisotropic refinements. (d) $Au_{24}S_{16}$ structure showing two Au_3SR_4 motifs, one Au_3SR_4 motif with green atoms on the right, another Au_3SR_4 motif with blue atoms on the left. (e) $Au_{24}S_{16}$ structure in (d) rotated by 90°, highlighting the orange Au atoms containing −Au−SR−Au−SR− motifs at top left and the pink Au atoms containing −Au−SR−Au−SR−Au−SR− motifs at bottom center. Coloring scheme: C, black; S, yellow; Au, red, blue, green, orange, and pink.

large nanomolecules were estimated by taking their average radius (R) and using the Born formula: $E_{solvation} = -(1 - 1/\varepsilon)/2R$, where ε is the dielectric constant of the solvent (ε = 38 for methanol). Madelung crystal energies were roughly estimated in the case of charged nanomolecules by applying the Born−Landé equation[40] with a distance between ions corresponding to the sum of the average radius R and the radius of a typical cationic counterion of ∼4 Å.

RESULTS AND DISCUSSION

X-ray Crystallography. Brown rhombic plate-like crystals suitable for X-ray analysis were obtained from a toluene:ethanol vapor−vapor diffusion setup. The nanomolecule crystallizes in a triclinic space group $P\bar{1}$, and was solved to an R_1 value of 5.19%. Figure 1a presents the total structure of $Au_{24}(SAdm)_{16}$, with the hydrogen atoms omitted for clarity. The central Au atom is surrounded by 12 Au atoms to form a Au_{13} distorted cubocatahedral core, Figure 1b. All Au and S atoms were refined anisotropically and are displayed as thermal ellipsoids in Figure 1c. The anisotropic refinement of carbon atoms was investigated but was not computationally stable, and the numerical refinement indicators did not show a substantial improvement. Therefore, the isotropic model of carbon atoms was retained to conserve data. The Au_{13} distorted core is capped by two Au atoms on two (100) square faces to form a Au_{15} bipyramidal motif. These two cap atoms are coordinated to seven other Au atoms and are part of the core, as noted before.[20] However, the Au_{13} cuboctahedron plus two cap Au atom description is retained to facilitate the structural description with a more familiar polyhedral shape. The Au_{13} cuboctahedral core is capped by two $-Au_3(SR)_4-$ motifs, shown by the blue atoms on the left, and the green atoms on the right in Figure 1d. The other five gold atoms are shown in Figure 1e, by the orange Au atoms on the top left, and the pink Au atoms in the bottom center. One of the orange and one of the pink Au atoms are part of the core as noted above, while the others form a $Au(SR)_2-$ and a $Au_2(SR)_3-$ motif, respectively. Significant efforts were made to identify the residual electron density in the experimental diffraction data so it can be included in the X-ray crystal structure model. Attempts to identify and model the possible counterions were not successful. Since there are no clear counterions, the charge state is expected to be neutral. The structural features including the cuboctahedral core, $-Au_3(SR)_4-$, were previously reported[20,21] for the $Au_{23}(SCy)_{16}$ and the $Au_{30}S(StBu)_{18}$ systems. Here, for the first time we observe the adaptability of the structure leading to a *flexible composition*, $Au_{24\pm1}(SAdm)_{16}$. Based on a detailed theoretical analysis, we then propose a coherent framework which rationalizes this adaptability and its relation to the icosahedral $Au_{25}(SR)_{18}$, *vide infra*.

The Au−Au bond distances between the central atom and the vertices of the cuboctahedra vary between 2.704 and 3.490 Å. Whereas the $Au_{center}-Au_{cubo}$ distance is 2.97 ± 0.21 Å, the $Au_{center}-Au_{ico}$ average distance in $Au_{25}(SR)_{18}$ is 2.79 Å. The average $Au_{cubo}-Au_{cubo}$ distance is 2.92 ± 0.19 Å (3.26 Å max; 2.68 Å min.). This shows the distorted and unsymmetrical nature of the cubocatahedral core. The average $Au_{cubo}-Au_{other}$ distance is 3.03 ± 0.22 Å (3.38 Å max; 2.66 Å min). The average $Au_{cubo}-Au_{other}$ distance is only ∼0.06 Å longer than the $Au_{cubo}-Au_{core}$ distance. This is in contrast to the a larger variation of 0.38 Å between $Au_{ico}-Au_{core}$ and $Au_{ico}-Au_{other}$ distance in the case of $Au_{25}(SR)_{18}$. For this reason, in the

dx.doi.org/10.1021/ja507738e | J. Am. Chem. Soc. 2014, 136, 14933−14940

present $Au_{24}(SAdm)_{16}$ case, not all outer Au−Au bonds have an aurophilic nature.

Mass Spectrometry. Complementary evidence for X-ray crystallographic composition, $Au_{24}(SAdm)_{16}$, was provided by ESI mass spectrometry on the nanomolecule crystals, obtained in step 3 of the synthetic procedure. Figure 2 shows one

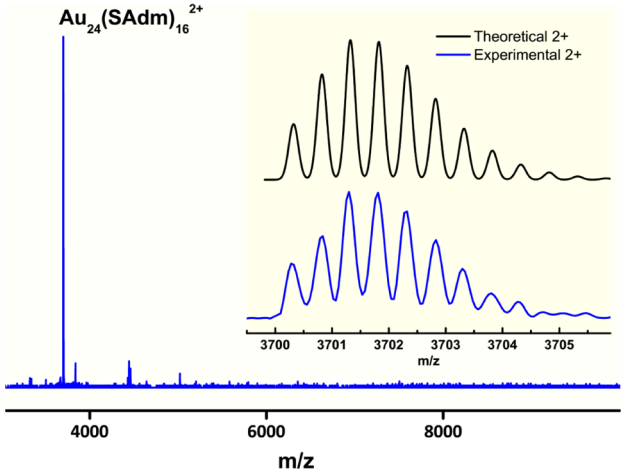

Figure 2. Electrospray ionization (ESI) mass spectrum of the crystalline material shows the 2+ ions at m/z 3701, corresponding to $Au_{24}(SAdm)_{16}$. Displayed in the inset are the experimental isotopic distribution pattern (bottom, blue) compared to that of theoretical isotopic pattern (top, black) for $Au_{24}(SAdm)_{16}$ composition.

dominant peak, m/z 3701, corresponding to the 2+ ions, as indicated by the isotopic mass difference, Δm = 0.5. The experimental isotopic blue pattern in the inset matches well with the calculated isotopic pattern in black corresponding to $Au_{24}(SAdm)_{16}$, confirming the crystallographic composition independently using mass spectrometry.

Optical Spectroscopy. The red spectrum in Figure 3 shows the UV−vis−NIR spectra of putative $Au_{24}(SAdm)_{16}$ crystals dissolved in toluene. The spectrum exhibits features at

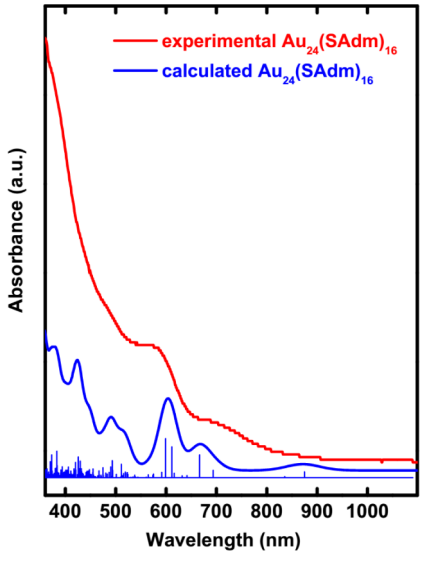

Figure 3. Experimental (red) UV−vis−NIR spectra of putative $Au_{24}(SAdm)_{16}$ crystals dissolved in toluene. The calculated TD-DFT spectra is shown in the blue curve.

580 and 690 nm, with a minor shoulder at 495 nm. The experimental works on $Au_{23}(SCy)_{16}$ and $Au_{30}(StBu)_{18}$ reports features at 570 and 620 nm, respectively.[20,21]

The theoretically predicted optical spectrum (blue curve) is also reported in Figure 3, and compares favorably with the experimental one. The simulated spectrum shows major features at 600 and 420 nm, as well as significant peaks at 495 and 665 nm, and minor features at 380 and 860 nm. Note that, in order to speed up TD-DFT calculations, these were conducted on model $Au_{24\pm1}(SMethyl)_{16}$ compounds in which the adamantyl ligands were replaced with methyl groups, as it is customary in modeling thiolated gold nanomolecules ligands.[41,42] An analysis of the electronic excitations in terms of occupied-virtual pairs allows us to interpret the low-energy transitions as associated with molecular orbitals with a strong Au(6s)/S(3p) mixed character. At such small sizes, the Au−S shell clearly dominates the optical response.[43,44] We can observe that the two low-energy peaks at 600 and 670 nm are determined by the same occupied-virtual pairs. The precise coupling of such intermingled excitations is obviously very difficult to predict accurately. Indeed, by recasting absorption in terms of excitation energies we notice that the experimental peaks fall at 2.14 and 1.80 eV, while simulations predict them at 2.07 and 1.87 eV: the spacing between the experimental peaks is thus larger than that of the calculated peaks by a factor of 1.6, but the center of the peak positions is identical from experiment and simulations, thus suggesting that disagreement between theory and experiment for this pair is due to an underestimation of the coupling between the excited states in simulations. Finally, in Figure S1 of the Supporting Information, the spectra of $Au_{23}(SMethyl)_{16}$ and $Au_{25}(SMethyl)_{16}$ are also reported to investigate the effects of adding or removing a Au atom on the optical properties of these nanomolecules. The peaks of such species are slightly shifted with respect to $Au_{24}(SMethyl)_{16}$, whence a predicted broadening can be expected when the experimental situation corresponds to a mixture of such species.

$Au_{23}(SAdm)_{16}$ and $Au_{25}(SAdm)_{16}$, and Theoretical Analysis of Its Relation to $Au_{24}(SAdm)_{16}$. The acetone-soluble fraction from step 2 of the synthetic procedure was analyzed by mass spectrometry. In contrast to the mass spectrum of the crystalline material shown in Figure 2, the acetone-soluble fraction in Figure 4 shows three peaks. In addition to the m/z 3701 peak corresponding to 2+ ions of $Au_{24}(SAdm)_{16}$, there were also two other peaks that were in the 1+ charge state, Δm = 1. These peaks at m/z 7203 and 7598 correspond to $Au_{23}(SR)_{16}$ and $Au_{25}(SR)_{16}$, as indicated by good isotopic distribution match with theoretical values, shown in the inset.

Figure 5 shows the X-ray crystal structures of $Au_{23}(SCy)_{16}$, $Au_{24}(SAdm)_{16}$ and the theoretical model of $Au_{25}(SAdm)_{16}$ optimized by DFT calculations. The top view has the blue and red $-Au_3(SR)_4-$ motifs in the plane of the paper. The bottom view is rotated by 90° and shows the structural changes. The addition of one Au pink atom to the Au_{23} structure leads to Au_{24} in the center: the added atom bridges two $-Au(SR)_2-$ motifs transforming them into an asymmetric $-Au_3(SR)_4-$ motif. Addition of a second Au orange atom to Au_{24} leads to the Au_{25} structure on the right, and is achieved again by bridging two $-Au(SR)_2-$ into a $-Au_3(SR)_4-$ motif. The sequential addition of Au atoms so singled out may possess a general character both in terms of structural analysis and growth mechanism.

dx.doi.org/10.1021/ja507738e | J. Am. Chem. Soc. 2014, 136, 14933−14940

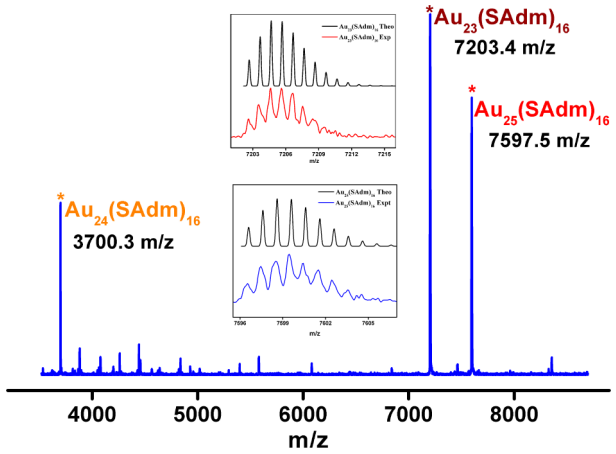

Figure 4. Mass spectrum of the acetone-soluble fraction in step 2, presenting evidence for the presence of $Au_{24\pm1}(SR)_{16}$. ESI mass spectrum of the 1+ ions corresponding to $Au_{23}(SAdm)_{16}$ and $Au_{25}(SAdm)_{16}$, in addition to the 2+ ions of $Au_{24}(SAdm)_{16}$.

Au_{13} Cuboctahedral *versus* Au_{13} Icosahedral Cores. Theoretical analysis can help us clarify the reasons of the preference toward the competing cuboctahedral vs icosahedral Au_{13} cores, with the former synthesized using bulky thiolate ligands and the latter using slimmer ligands as in $Au_{25}(SCH_2CH_2Ph)_{18}$.[7,45,46] It is appropriate to recall that—remarkably—in early pioneering work on a 29 kDa Au:SR compound, now commonly accepted as $Au_{144}(SR)_{60}$, Whetten and co-workers suggested that the core structure depends on ligand shell.[47] Clearly, on those larger systems lacking X-ray characterization, it was impossible to achieve the level of atomistically detailed evidence that is presented here. We believe that a combination of experimental and theoretical efforts should eventually aim at drawing a thermodynamic phase diagram of gold nanomolecules as a function of the system variables: number of Au atoms, charge, strength of S−H bond and steric hindrance of the thiolate ligand, and environmental conditions (polarizability and dispersion/repulsion contributions of the solvent medium, and strength of the reducing agent). In the Supporting Information we thus provide additional information and analysis that can be useful in this perspective, while a synthetic analysis is reported here. From previous work,[46] we derive the main conclusion that *local chemical bonding* and *surface coverage effects* dominate the system energetics and are much more important than global electronic structure contributions such as electronic shell closure effects (this is even truer in the present case of only eight metallic electrons), and we follow a similar line of reasoning. However, for the sake of simplicity, we choose somewhat difference reference states in our thermodynamic analysis. We then consider the following reactions:

$$Au_N(SR)_{16(s)} + Au^+_{(s)} + Rd^-_{(s)} \rightarrow Au_{N+1}(SR)_{16(s)} + Rd_{(s)} \quad (1)$$

$$Au_N(SR)_{16(s)} + Rd^-_{(s)} \rightarrow Au_N(SR)_{16}{}^-_{(s)} + Rd_{(s)} \quad (2)$$

where Rd is a generic reducing agent and the subscript "(s)" indicates that the corresponding species are in solution. Equations 1 and 2 can be formally decomposed into the following steps:

$$Au^+_{(s)} + e^-_{(inf)} \rightarrow Au_{(inf)} \quad (3)$$

$$Rd^-_{(s)} \rightarrow Rd_{(s)} + e^-_{(inf)} \quad (4)$$

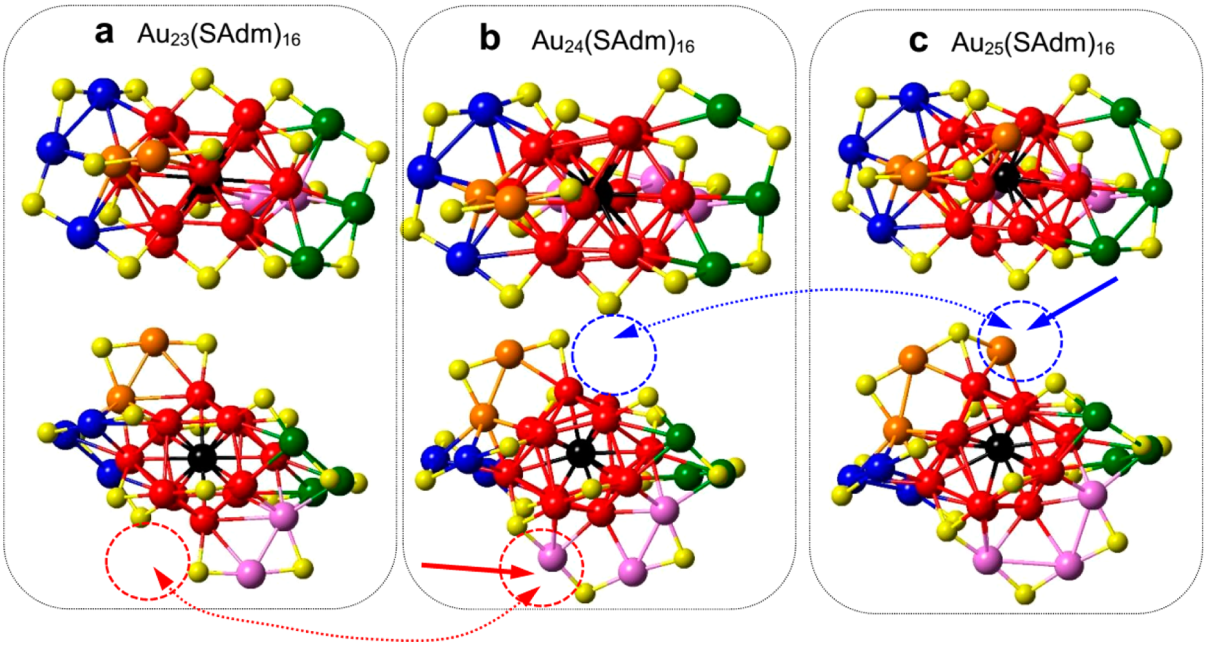

Figure 5. Adaptability in the atomic structure for a flexible composition, $Au_{24\pm1}$ to form Au_{23}, Au_{24} and Au_{25}: (a) X-ray structure of $Au_{23}S_{16}$ from the $Au_{23}(SCy)_{16}$ (ref 20); (b) X-ray structure of $Au_{24}S_{16}$ from this work; (c) $Au_{25}S_{16}$ theoretical model optimized by DFT calculations. The bottom images are rotated by 90 deg in the plane of the paper. The structural changes between Au_{23}, Au_{24} and Au_{25} are easily visualized in the bottom images. Au_{24} is formed by the addition of one Au atom to Au_{23} indicated by the red solid and dotted arrows. Au_{25} is formed by addition of one Au atom to Au_{24} indicated by the blue colored solid and dotted arrows. Note that the number of ligands, 16, is constant in all three structures. Smaller yellow atoms are sulfur and all other atoms are Au. C and H are omitted for clarity.

dx.doi.org/10.1021/ja507738e | J. Am. Chem. Soc. 2014, 136, 14933−14940

$$Au_N(SR)_{16(s)} + Au_{(inf)} \rightarrow Au_{N+1}(SR)_{16(s)} \quad (5)$$

$$Au_N(SR)_{16(s)} + e^-_{(inf)} \rightarrow Au_N(SR)_{16}{}^-_{(s)} \quad (6)$$

where the subscript "(inf)" indicates that the corresponding species are isolated in vacuum (infinity) and at rest, a state taken as a reference for convenience. The sum of reactions 3 and 4 corresponds to minus the chemical potential of a neutral Au atom, while eq 4 corresponds to the chemical potential of a reducing electron in the reaction medium. From DFT total energy calculations, we derive values of the incremental formation energy (IFE) of $Au_N(SR)_{16}$ compounds, eq 5, and of their electron affinity (EA), eq 6, and we report them in Table 1. By estimating the chemical potentials of $Au_{(inf)}$ and of a reducing electron under the given conditions, and IFE and EA values from Table 1, we can immediately derive the reaction energies of processes 1 and 2. For example, in the Supporting Information we derive the chemical potentials of $Au_{(inf)}$ and of a reducing electron as +0.02 and +0.29 Ry, respectively, assuming certain experimental conditions (see the SI for more details).

Table 1. DFT Energetics of the Au Nanomolecules Considered in This Work[a]

system	energy	23, 16	24, 16	25, 16	25, 18
adamantyl	TFE	−4.71	−5.06	−5.11	−5.06
	EA	−0.18	−0.07	−0.11	−0.13
	IFE		−0.35	−0.05	
cyclohexyl	TFE	−4.94	−5.18	−5.30	−5.29
	EA	−0.21	−0.10	−0.08	−0.16
	IFE		−0.24	−0.12	
methyl	TFE	−4.83	−5.07	−5.11	−5.30
	EA	−0.26	−0.15	−0.22	−0.22
	IFE		−0.24	−0.04	
phenylethyl	TFE			−5.21	−5.39
	EA			−0.13	−0.17

[a]The following energy quantities are reported: TFE, total formation energy; EA, electron affinity; IFE, incremental formation energy. Energies are reported in Ry.

To compare the stability of gold nanomolecules coated by different ligands, not only incremental processes but also total formation energies (TFE) need to be considered, which we estimate via the process:

$$N\,Au_{(inf)} + 16RSH_{(inf)} \rightarrow Au_N(SR)_{16(s)} + 8H_{2(inf)} \quad (7)$$

An analogous equation holds in the case of $Au_N(SR)_{18}$ species. Equation 7 involves the chemical potential of the thiol RSH in terms of strength of the RS−H bond, which is also reported in Table S1 of the SI. For a further energy decomposition, we provide in Table S1 the reaction energies of the following processes:

$$N\,Au_{(inf)} \rightarrow Au_{N(inf)} \quad (8)$$

$$Au_{N(inf)} + (SR)_{16(inf)} \rightarrow Au_N(SR)_{16(s)} \quad (9)$$

$$16RS_{(inf)} \rightarrow (SR)_{16(inf)} \quad (10)$$

$$16RSH_{(inf)} \rightarrow 16RS_{(inf)} + 16H_{(inf)} \quad (11)$$

$$16H_{(inf)} \rightarrow 8H_{2(inf)} \quad (12)$$

where eq 8 corresponds to atomization of the Au cluster frozen in its interacting configuration, eq 9 corresponds to decomposition of the nanomolecule into Au clusters and thiolate ligands, both frozen in their interacting configurations. Equation 10 corresponds to the interaction of thiolate ligands in their interacting configuration and is meant to provide an estimate of *steric repulsion* (even though it includes some RS-SR bond energy). Note that the reaction energy of eq 7 is the sum of reaction energies of eqs 8−12.

Three main conclusions can be drawn from an analysis of the data reported in Table 1.

First, the transition from $Au_{25}(SCH_2CH_2Ph)_{18}$ to $Au_{23-25}(SCy)_{16}$ or $Au_{23-25}(SAdm)_{16}$ is clearly explained as due to the steric repulsion among the bulky cyclohexyl (SCy) or adamantyl (SAdm) ligands. Indeed, the TFE of $Au_{25}(SR)_{18}$ is *smaller* than that of $Au_{25}(SR)_{16}$, when R = adamantlyl or cyclohexyl, whereas it is *much larger* for R = methyl or phenylethyl. From the values of Table S1 of the SI, we can also see that the interaction between ligands is repulsive in the case of $Au_{23}(SAdm)_{16}$, +0.08 Ry, whereas it is much smaller in the case of $Au_{23}(SCy)_{16}$ and even attractive in the case of $Au_{23}(SMe)_{16}$. At variance with cyclohexyls, adamantyls are so bulky that a significant steric repulsion is still present in $Au_{23}(SAdamantyl)_{16}$, thus explaining its instability. The situation changes when adding an Au atom: the repulsion between adamantyl ligands drops to +0.01 Ry only and $Au_{24}(SAdm)_{16}$ is an extremely stable species. Steric considerations finally disfavor the $Au_{25}(SAdm)_{18}$ complex, where the greater number of gold atoms does not succeed in decreasing the repulsion between the 18 adamantyl groups (+0.11 Ry).

Second, it can be observed that cyclohexanethiolate and methanethiolate $Au_N(SR)_{16}$ nanomolecules exhibit a similar energetics at size N = 23, 24 but not at N = 25. Because the steric hindrance is also similar (see Table S1 of the SI), this confirms[46] that local chemical bonding and surface coverage effects finally determine the energetics of these systems. In passing, it can be noted that a significant difference between the energetics of the two ligands lies in a difference in S−H bond strength of some 3.2 kcal/m between cyclohexanethiol and methylthiol, with adamantanethiol presenting an intermediate S−H bond strength. This does not seem to be decisive in the present case, but may play a role in other systems.

Third, for the process of the reduction of gold nanomolecules, eq 2, to be favorable, the electron affinity of $Au_N(SR)_{16}$ must overcome the chemical potential of an electron in the reaction medium minus the solvation energy of the resulting charged species. If the value of 0.22 Ry from the SI is taken as chemical potential of the electron, the species here considered are all predicted to be neutral in solution under the given conditions, with the exception of $Au_{23}(SMe)_{16}$ and the near energetic neutrality for $Au_{23}(SCy)_{16}$, $Au_{25}(SMe)_{16}$, and $Au_{25}(SMe)_{18}$. Additionally, it can be noted that the estimated Madelung energy of ∼0.12 Ry (see the Supporting Information) is larger than the solvation energy of the nanomolecular anion and can overcome such energy penalty, and this indeed explains why experimentally the $Au_{23}(SCy)_{16}$ nanomolecule is charged in the crystal. In contrast, the $Au_{24}(SR)_{16}$ species are expected to crystallize as neutrals, as indeed found by the absence of counterions for $Au_{24}(SAdm)_{16}$. The observed even−odd alternation in electron affinity as a function of the number of Au atoms[48] explains in part the

dx.doi.org/10.1021/ja507738e | J. Am. Chem. Soc. 2014, 136, 14933−14940

trends observed in Table 1, even though local chemical bonding and surface coverage effects[46] subtly tune the system energetics. Note that the presence of 2+ cations in the mass spectrum of Figure 4 may be due to ionization efficiency rather than to a different charge state of the $Au_{23,25}(SAdm)_{16}$ with respect to $Au_{24}(SAdm)_{16}$ compounds.

Of course, these thermodynamic estimates given can be refined, especially in terms of solvation effects. Nevertheless, the results of the theoretical analysis are well in tune with experiment, beginning with the transition from $Au_{25}(SR)_{18}$ to $Au_{23,24}(SR)_{16}$ when passing from slim to bulky thiolate ligands. Moreover, in the case of the adamantyl ligand, the superior stability of $Au_{24}(SAdm)_{16}$ is associated with the steric hindrance in $Au_{23}(SAdm)_{16}$ on the one hand, and the modest increase in metal bonding in $Au_{25}(SAdm)_{16}$ on the other hand. Despite this, the presence of Au_{23} and Au_{25} compounds in the reaction moiety is not excluded from an energetic point of view, and indeed is observed in the mass spectra in Figure 4. It can be argued that this is also the case for the homologous $Au_{23}(SCy)_{16}$ system, although not highlighted in ref 20. We finally note the recent reports[49,50] on $Au_{24}(SCH_2Ph\text{-}tBu)_{20}$ and $Au_{24}(SePh)_{20}$. The crystal structure of $Au_{24}(SAdm)_{16}$ is unique and unrelated to these other recently published 24-atom crystal structures.

CONCLUSIONS

In summary, we have conducted a combined experimental and theoretical investigation of $Au_x(SR)_y^q$ nanomolecules with x = 23−25, y = 16, 18, q = 0, −1, as a function of thiolate groups, with specific attention to the consequences of steric hindrance of thiolates upon structure and stoichiometry of these systems. One main result is that—switching from slim alkyl ligands to bulky adamantyl ones—the previously observed transition from icosahedral to fcc-like configurations is shown to entail a much greater structural and stoichiometric liberty for the latter compounds. Experimentally, we were able to isolate a novel $Au_{24}(SR)_{16}$ nanomolecule, and characterize the crystalline specimens via optical spectroscopy and X-ray crystallography. However, ESI spectrometry of the crude acetone-soluble fractions shows the presence in the solvated phase before crystallization of $Au_{23,25}(SR)_{16}^q$ species as well. This is rationalized via a detailed analysis of the energetics of these systems as predicted by first-principles simulations which, also expanded to include cyclohexyl[19] and methyl[8] ligands, (i) outlines a growth pattern in terms of $-Au_3(SR)_4-$ motifs of increasing length and (ii) predicts a crossover among the various competing species in solution, $Au_x(SR)_{16}^q$ (x = 23−25) and $Au_{25}(SR)_{18}^q$, both neutral and negatively charged (q = 0, −1), as a function of few basic parameters: strength of RS−H bond, steric hindrance of thiolate ligand, and environmental conditions (solvation features of the medium, chemical potential of reducing electron). Local chemical bonding and surface coverage effects[46] are also confirmed to subtly tune the system energetics. In such a complex landscape, thermodynamic considerations provide a useful framework in which to place experimental findings, rationalizing, e.g., the preference for $Au_{24}(SAdm)_{16}$ neutral species with respect to $Au_{23,25}(SAdm)_{16}$ or $Au_{24}(SAdm)_{18}$ anions, and similarly when changing the nature of the thiolate ligand. Deriving a thermodynamic phase diagram of Au nanomolecule systems thus seems to be a valuable aid to orient the synthesis of Au nanomolecules, although kinetic phenomena such as growth or crystallization mechanisms or ionization efficiency are found to also play a role in determining heuristic fine details.

ASSOCIATED CONTENT

Supporting Information

Simulated TD-DFT spectra and crystal data. CCDC number 996445. This material is available free of charge via the Internet at http://pubs.acs.org.

AUTHOR INFORMATION

Corresponding Authors

alessandro.fortunelli@cnr.it
amal@olemiss.edu

Notes

The authors declare no competing financial interest.

ACKNOWLEDGMENTS

NSF-CHE-1255519 supported the work performed by D.C. and A.D. We thank Asantha Dharmaratne for assistance with testing synthesis reproducibility.

REFERENCES

(1) Whetten, R. L.; Khoury, J. T.; Alvarez, M. M.; Murthy, S.; Vezmar, I.; Wang, Z. L.; Stephens, P. W.; Cleveland, C. L.; Luedtke, W. D.; Landman, U. *Adv. Mater.* **1996**, *8*, 428.
(2) Templeton, A. C.; Wuelfing, M. P.; Murray, R. W. *Acc. Chem. Res.* **2000**, *33*, 27.
(3) Maity, P.; Xie, S.; Yamauchi, M.; Tsukuda, T. *Nanoscale* **2012**, *4*, 4027.
(4) Niihori, Y.; Matsuzaki, M.; Pradeep, T.; Negishi, Y. *J. Am. Chem. Soc.* **2013**, *135*, 4946.
(5) Pei, Y.; Zeng, X. C. *Nanoscale* **2012**, *4*, 4054.
(6) Jadzinsky, P. D.; Calero, G.; Ackerson, C. J.; Bushnell, D. A.; Kornberg, R. D. *Science* **2007**, *318*, 430.
(7) Heaven, M. W.; Dass, A.; White, P. S.; Holt, K. M.; Murray, R. W. *J. Am. Chem. Soc.* **2008**, *130*, 3754.
(8) Chen, S. W.; Murray, R. W. *Langmuir* **1999**, *15*, 682.
(9) Chaki, N. K.; Negishi, Y.; Tsunoyama, H.; Shichibu, Y.; Tsukuda, T. *J. Am. Chem. Soc.* **2008**, *130*, 8608.
(10) Nimmala, P. R.; Yoon, B.; Whetten, R. L.; Landman, U.; Dass, A. *J. Phys. Chem. A* **2013**, *117*, 504.
(11) Dainese, T.; Antonello, S.; Gascón, J. A.; Pan, F.; Perera, N. V.; Ruzzi, M.; Venzo, A.; Zoleo, A.; Rissanen, K.; Maran, F. *ACS Nano* **2014**, *8*, 3904.
(12) Kumara, C.; Zuo, X.; Ilavsky, J.; Chapman, K. W.; Cullen, D. A.; Dass, A. *J. Am. Chem. Soc.* **2014**, *136*, 7410.
(13) Kumara, C.; Zuo, X.; Cullen, D. A.; Dass, A. *ACS Nano* **2014**, *8*, 6431.
(14) Kumara, C.; Dass, A. *Anal. Chem.* **2014**, *86*, 4227.
(15) Nimmala, P. R.; Dass, A. *J. Am. Chem. Soc.* **2011**, *133*, 9175.
(16) Qian, H.; Eckenhoff, W. T.; Zhu, Y.; Pintauer, T.; Jin, R. *J. Am. Chem. Soc.* **2010**, *132*, 8280.
(17) Zeng, C.; Qian, H.; Li, T.; Li, G.; Rosi, N. L.; Yoon, B.; Barnett, R. N.; Whetten, R. L.; Landman, U.; Jin, R. *Angew. Chem., Int. Ed.* **2012**, *51*, 13114.
(18) Krommenhoek, P. J.; Wang, J.; Hentz, N.; Johnston-Peck, A. C.; Kozek, K. A.; Kalyuzhny, G.; Tracy, J. B. *ACS Nano* **2012**, *6*, 4903.
(19) Nishigaki, J.-i.; Tsunoyama, R.; Tsunoyama, H.; Ichikuni, N.; Yamazoe, S.; Negishi, Y.; Ito, M.; Matsuo, T.; Tamao, K.; Tsukuda, T. *J. Am. Chem. Soc.* **2012**, *134*, 14295.
(20) Das, A.; Li, T.; Nobusada, K.; Zeng, C.; Rosi, N. L.; Jin, R. *J. Am. Chem. Soc.* **2013**, *135*, 18264.
(21) Crasto, D.; Malola, S.; Brosofsky, G.; Dass, A.; Häkkinen, H. *J. Am. Chem. Soc.* **2014**, *136*, 5000.
(22) Hesari, M.; Workentin, M. S. *J. Mater. Chem. C* **2014**, *2*, 3631.
(23) Crasto, D.; Dass, A. *J. Phys. Chem. C* **2013**, *117*, 22094.

(24) Schaaff, T. G.; Whetten, R. L. *J. Phys. Chem. B* **1999**, *103*, 9394.
(25) Dolomanov, O. V.; Bourhis, L. J.; Gildea, R. J.; Howard, J. A. K.; Puschmann, H. *J. Appl. Crystallogr.* **2009**, *42*, 339.
(26) Giannozzi, P.; et al. *J. Phys.: Condens. Matter* **2009**, *21*, 395502.
(27) Vanderbilt, D. *Phys. Rev. B* **1990**, *41*, 7892.
(28) Perdew, J. P.; Burke, K.; Ernzerhof, M. *Phys. Rev. Lett.* **1996**, *77*, 3865.
(29) Hutter, J.; Iannuzzi, M.; Schiffmann, F.; VandeVondele, J. *WIREs Comput. Mol. Sci.* **2014**, *4*, 15.
(30) Lippert, G.; Hutter, J.; Parrinello, M. *Theor. Chem. Acc.* **1999**, *103*, 124.
(31) Goedecker, S.; Teter, M.; Hutter, J. *Phys. Rev. B* **1996**, *54*, 1703.
(32) VandeVondele, J.; Hutter, J. *J. Chem. Phys.* **2007**, *127*, 114105.
(33) Martyna, G. J.; Klein, M. L.; Tuckerman, M. *J. Chem. Phys.* **1992**, *97*, 2635.
(34) Baerends, E. J.; Ellis, D. E.; Ros, P. *Chem. Phys.* **1973**, *2*, 41.
(35) Fonseca Guerra, C.; Snijders, J. G.; te Velde, G.; Baerends, E. J. *Theor. Chem. Acc.* **1998**, *99*, 391.
(36) Cadsida, M. E. In *Recent Advances in Density-Functional Methods*; Chong, D. P., Ed.; World Scientific: Singapore, 1995; p 155.
(37) van Leeuwen, R.; Baerends, E. J. *Phys. Rev. A* **1994**, *49*, 2421.
(38) Frisch, M. J.; Trucks, G. W.; Schlegel, H. B.; Scuseria, G. E.; Robb, M. A.; Cheeseman, J. R.; Scalmani, G.; Barone, V.; Mennucci, B.; Petersson, G. A.; Nakatsuji, H.; Caricato, M.; Li, X.; Hratchian, H. P.; Izmaylov, A. F.; Bloino, J.; Zheng, G.; Sonnenberg, J. L.; Hada, M.; Ehara, M.; Toyota, K.; Fukuda, R.; Hasegawa, J.; Ishida, M.; Nakajima, T.; Honda, Y.; Kitao, O.; Nakai, H.; Vreven, T.; Montgomery, J. A., Jr.; Peralta, J. E.; Ogliaro, F.; Bearpark, M. J.; Heyd, J.; Brothers, E. N.; Kudin, K. N.; Staroverov, V. N.; Kobayashi, R.; Normand, J.; Raghavachari, K.; Rendell, A. P.; Burant, J. C.; Iyengar, S. S.; Tomasi, J.; Cossi, M.; Rega, N.; Millam, N. J.; Klene, M.; Knox, J. E.; Cross, J. B.; Bakken, V.; Adamo, C.; Jaramillo, J.; Gomperts, R.; Stratmann, R. E.; Yazyev, O.; Austin, A. J.; Cammi, R.; Pomelli, C.; Ochterski, J. W.; Martin, R. L.; Morokuma, K.; Zakrzewski, V. G.; Voth, G. A.; Salvador, P.; Dannenberg, J. J.; Dapprich, S.; Daniels, A. D.; Farkas, Ö.; Foresman, J. B.; Ortiz, J. V.; Cioslowski, J.; Fox, D. J. *Gaussian09*; Gaussian, Inc.: Wallingford, CT, 2009.
(39) Hay, P. J.; Wadt, W. R. *J. Chem. Phys.* **1985**, *82*, 299.
(40) Brown, I. D. *The Chemical Bond in Inorganic Chemistry: The Bond Valence Model*, reprint. ed.; Oxford University Press: New York, 2002.
(41) Knoppe, S.; Malola, S.; Lehtovaara, L.; Bürgi, T.; Häkkinen, H. *J. Phys. Chem. A* **2013**, *117*, 10526.
(42) Häkkinen, H. *Nat. Chem.* **2012**, *4*, 443.
(43) Malola, S.; Lehtovaara, L.; Enkovaara, J.; Häkkinen, H. *ACS Nano* **2013**, *7*, 10263.
(44) Aikens, C. M. *J. Phys. Chem. C* **2008**, *112*, 19797.
(45) Parker, J. F.; Fields-Zinna, C. A.; Murray, R. W. *Acc. Chem. Res.* **2010**, *43*, 1289.
(46) Reimers, J. R.; Wang, Y.; Cankurtaran, B. O.; Ford, M. J. *J. Am. Chem. Soc.* **2010**, *132*, 8378.
(47) Schaaff, T. G.; Shafigullin, M. N.; Khoury, J. T.; Vezmar, I.; Whetten, R. L. *J. Phys. Chem. B* **2001**, *105*, 8785.
(48) Grönbeck, H.; Rosén, A. *Z. Phys. D: At., Mol. Clusters* **1996**, *36*, 153.
(49) Song, Y.; Wang, S.; Zhang, J.; Kang, X.; Chen, S.; Li, P.; Sheng, H.; Zhu, M. *J. Am. Chem. Soc.* **2014**, *136*, 2963.
(50) Das, A.; Li, T.; Li, G.; Nobusada, K.; Zeng, C.; Rosi, N. L.; Jin, R. *Nanoscale* **2014**, *6*, 6458.